Subseasonal SST Variability in the Tropical Eastern North Pacific during Boreal Summer

ERIC D. MALONEY, DUDLEY B. CHELTON, AND STEVEN K. ESBENSEN

College of Oceanic and Atmospheric Sciences, Oregon State University, Corvallis, Oregon

ABSTRACT

Boreal summer intraseasonal (30–90-day time scale) sea surface temperature (SST) variability in the east Pacific warm pool is examined using Tropical Rainfall Measuring Mission (TRMM) Microwave Imager (TMI) sea surface temperatures during 1998–2005. Intraseasonal SST variance maximizes at two locations in the warm pool: in the vicinity of 9°N, 92°W near the Costa Rica Dome and near the northern edge of the warm pool in the vicinity of 19°N, 108°W. Both locations exhibit a significant spectral peak at 50–60-day periods, time scales characteristic of the Madden–Julian oscillation (MJO). Complex empirical orthogonal function (CEOF) and spectra coherence analyses are used to show that boreal summer intraseasonal SST anomalies are coherent with precipitation anomalies across the east Pacific warm pool. Spatial variations of phase are modest across the warm pool, although evidence exists for the northward progression of intraseasonal SST and precipitation anomalies. Intraseasonal SSTs at the north edge of the warm pool lag those in the vicinity of the Costa Rica Dome by about 1 week.

The MJO explains 30%–40% of the variance of intraseasonal SST anomalies in the east Pacific warm pool during boreal summer. Peak-to-peak SST variations of 0.8°–1.0°C occur during MJO events. SST is approximately in quadrature with MJO precipitation, with suppressed (enhanced) MJO precipitation anomalies leading positive (negative) SST anomalies by 7–10 days. Consistent with the CEOF and coherence analyses, MJO-related SST and precipitation anomalies near the Costa Rica Dome lead those at the northern edge of the warm pool by about 1 week.

1. Introduction

The Madden–Julian oscillation (MJO; Madden and Julian 2005) produces a significant modulation of boreal summer winds, precipitation, and surface fluxes in the east Pacific warm pool, where local processes appear to amplify these wind and precipitation anomalies (e.g., Molinari et al. 1997; Kayano and Kousky 1999; Maloney and Hartmann 2000; Higgins and Shi 2001; Maloney and Esbensen 2003; de Szoeke and Bretherton 2005; Raymond et al. 2006; Lorenz and Hartmann 2006). Maloney and Esbensen (2007, hereafter ME07) found that a significant positive covariance occurs between MJO precipitation and latent heat flux in the east Pacific warm pool during boreal summer, with an enhancement of latent heat flux occurring in association with MJO surface westerly wind anomalies and enhanced precipitation. We loosely define the tropical northeast Pacific "warm pool" as the area to the east of 120°W contained within the 28°C isotherm, as evident in a map of June–October average sea surface temperature (SST; Fig. 1). While some debate exists as to whether the warm summertime oceans of the tropical northeast Pacific can be treated as a separate warm pool from the Gulf of Mexico and the Caribbean Sea (e.g., Wang and Enfield 2001; Magaña and Caetano 2005), we will treat the east Pacific warm pool as independent for the purposes of this paper, because intraseasonal SST variability is concentrated there.

Significant east Pacific warm pool SST variations have been documented to occur in association with the boreal summer MJO (Maloney and Kiehl 2002a, hereafter MK02). MK02 used the Reynolds and Smith (1994) weekly averaged SST dataset to show that composite peak-to-peak variations of 0.4°–0.5°C occur during an MJO life cycle, and SST anomalies are in quadrature with MJO precipitation, with suppressed (enhanced) precipitation leading positive (negative) SST anomalies by 1–2 weeks. National Centers for Environ-

Corresponding author address: Eric D. Maloney, Dept. of Atmospheric Science, Colorado State University, 1371 Campus Delivery, Fort Collins, CO 80523-1371.
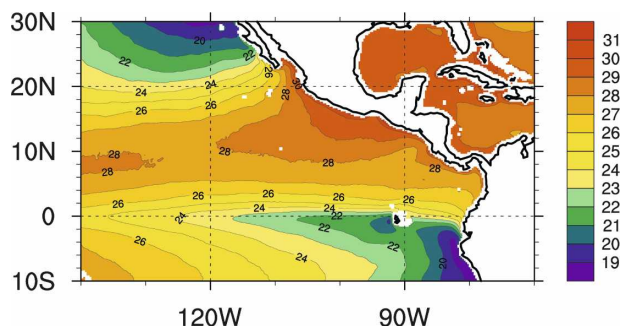E-mail: emaloney@atmos.colostate.edu

FIG. 1. Mean June–October TMI SST during 1998–2005. The contour interval is 1°C.

mental Prediction (NCEP)–National Center for Atmospheric Research (NCAR) reanalysis data suggest that these warm pool SST anomalies may be generated by local anomalous air–sea fluxes of latent heat and shortwave radiation operating on average summertime mixed layer depths (MK02). The analysis of MK02 based on the Reynolds and Smith (1994) SST analyses and NCEP reanalysis winds also suggests that the boreal summer MJO is associated with cold tongue SST anomalies of opposite sign to those in the warm pool. Local air–sea heat exchange does not appear to explain such equatorial anomalies, which may exist in large part through ocean dynamical feedbacks to anomalous equatorial wind stress, including remote forcing of the equatorial oceanic waveguide and subsequent Kelvin wave propagation into the east Pacific (e.g., Spillane et al. 1987; Enfield 1987; Zhang 2001; McPhaden 2002).

Our use of Tropical Rainfall Measuring Mission (TRMM) Microwave Imager (TMI) SST data to understand east Pacific intraseasonal SST variability is motivated by previous theoretical, modeling, and observational evidence suggesting that intraseasonal SST variability provides important feedbacks onto atmospheric convection. For example, idealized column models, such as those used in Sobel and Gildor (2003) and Maloney and Sobel (2004), suggest that atmosphere–ocean coupling can generate strong, local intraseasonal oscillations having a discharge/recharge character. Oceanic heat content builds before an intraseasonal convective event and is discharged during the convective event through enhanced latent heat fluxes and suppressed net downward surface shortwave radiation. For mixed layer depths that are plausible values for the east Pacific, the model of Sobel and Gildor (2003) produces realistic intraseasonal precipitation anomalies with peak-to-peak SST variations of 1°–1.5°C. Further, Maloney and Kiehl (2002b), using a general circulation model, showed that ocean coupling can amplify MJO-related precipitation variability in the east Pacific, al-

though results from this study were not entirely conclusive because intraseasonal SST and precipitation were in phase rather than in quadrature as in observations. The importance of ocean coupling to intraseasonal convective variability is also an open question on a global basis (e.g., Waliser et al. 1999; Hendon 2000). Accurate observational analyses of intraseasonal SST phase and amplitude should help to determine whether such variability is important for supporting east Pacific intraseasonal convection.

Previous studies such as Chelton (2005) and Chelton and Wentz (2005) have shown that the Reynolds SST product used in MK02 to study the MJO severely underestimates the amplitude of intraseasonal SST features on a global basis. The Reynolds and Smith (1994) product combines Advanced Very High Resolution Radiometer (AVHRR) SST retrievals with ship and buoy measurements of ocean temperature to generate a weekly averaged global SST analysis. The AVHRR measurements are of limited use for retrieving SST in cloudy regions, a deficiency particularly problematic for studying regions containing strong MJO-precipitation variability. A further deficiency to the Reynolds SST product discussed in Chelton (2005) and Chelton and Wentz (2005) is that this SST dataset is derived using long spatial correlation length scales, which act as a strong spatial smoother to limit the influence of poorly sampled SST variability with small spatial scales.[1] The present study analyzes intraseasonal SST variability in the east Pacific during boreal summer using the SST dataset from the TMI (Wentz et al. 2000). SST retrievals from the TMI are relatively unaffected by clouds, aerosols, and water vapor (Wentz et al. 2000), and thus are better suited for studying SST in regions of strong convective variability associated with the MJO. Recent studies of the MJO in the Indian Ocean using TMI SST suggest that the Reynolds SST product may underestimate SST variability there (Harrison and Vecchi 2001; Sengupta et al. 2001; Bhat et al. 2004).

As described below, the intraseasonal SST anomalies that dominate our analysis have phase variations with zonal scales on the same order as the east Pacific warm pool, although substantial finescale variations in amplitude occur. Associated in large part with the MJO, these SST variations have characteristic zonal scales that are at least a factor of 4 greater than oceanic eddies

---

[1] The correlation length scales used in the Reynolds and Smith (1994) SST analyses have recently been shortened to produce new AVHRR-based SST analyses with a much higher spatial resolution (Reynolds et al. 2007). These newly available SST fields show great promise but have not yet been validated in the region of interest in this study.

(e.g., Wijesekera et al. 2005; Palacios and Bogard 2005) and oceanic Rossby waves (e.g., Farrar and Weller 2006) that also produce intraseasonal variations in SST in the east Pacific warm pool. MJO-related intraseasonal SST variability in the east Pacific is also distinguishable in space and time scales from that of oceanic tropical instability waves, which have a maximum variance near 1°N (Legeckis 1977; Qiao and Weisberg 1995; Chelton et al. 2000, 2001; Hashizume et al. 2001). The midsummer drought (e.g., Magaña et al. 1999; Curtis 2002; Magaña and Caetano 2005; Small et al. 2007), a climatological intraseasonal oscillation in boreal summer precipitation in the Americas, is also associated with SST variability of spatial scale comparable to that of the east Pacific warm pool. However, as we will demonstrate below, the MJO-related SST variability that we study has a shorter time scale than the characteristic 90–100-day periods of the midsummer drought. Our analysis will also emphasize SST variability relative to the climatological seasonal cycle, and thus minimize the influence of the midsummer drought.

The organization of the paper is as follows: section 2 describes the datasets used in this study; section 3 presents an analysis of variance and coherence of boreal summer intraseasonal SST and precipitation in the east Pacific warm pool. Complex empirical orthogonal function (CEOF) analysis is used to examine the covariability of intraseasonal SST and precipitation in section 4. Section 5 uses an equatorial zonal wind MJO time series to examine how east Pacific SST and precipitation vary during MJO events. Section 6 presents discussion and conclusions.

2. Data

a. Sea surface temperature

Daily averaged gridded TMI SST data (version 4; Wentz et al. 2000) were obtained from Remote Sensing Systems (http://www.ssmi.com). The TMI footprint size is 46 km. The data are provided on a 0.25° × 0.25° latitude–longitude grid. SST data during June–October of 1998–2005 are used in the analysis, although an extended May–October period is used for calculation of the spectra, so that MJO time scales can be better distinguished from the 90–100-day periods of the climatological midsummer drought. Gentemann et al. (2004) note that daily averaged TMI SST data may contain substantial high-frequency noise caused by algorithm errors, instrument noise, and/or incomplete daily sampling (due to satellite overpass frequency and rain contamination). Thus, for most of the analyses described below, we preprocess the SST fields using spatial and temporal averaging to minimize the influence of such

high-frequency noise. We use data on the 0.25° × 0.25° grid only to present mean June–October SST in Fig. 1. For the rest of our analysis, the following data processing is used. First, at each 0.25° × 0.25° grid cell, SST anomalies of magnitude greater than 1.75 times the 60-day running standard deviation are removed. On average, less than 5% of the observations are removed at individual 0.25° × 0.25° grid cells in the east Pacific warm pool using such screening. Next, SST observations are averaged onto a 1° × 1° grid and then composited as overlapping 3-day averages at daily intervals to mitigate the effects of missing data from the sampling pattern of the TMI and from rain contamination of individual measurements. Less than 2% of the resulting daily SST composites were missing during June–October in the ITCZ, and less than 1% were missing outside the ITCZ, even during periods of enhanced intraseasonal precipitation variability. Any missing SST values were then filled by linear interpolation in time. As described below, our preprocessing technique produces a TMI dataset with intraseasonal SST anomalies of similar phase and amplitude to those from Tropical Atmosphere Ocean (TAO) buoys and the Advanced Microwave Scanning Radiometer for Earth Observing System (EOS; AMSR-E; e.g., Chelton and Wentz 2005). Thus, we are confident in the ability of the TMI SST product to fully represent the SST variability associated with intraseasonal oscillations in the east Pacific warm pool during summertime, which is the focus of this study.

We also briefly use the Reynolds SST dataset (Reynolds et al. 2002) during 1998–2005 as a comparison with the TMI data. As noted in the introduction, the Reynolds dataset combines AVHRR SST retrievals with ship and buoy measurements of ocean temperature to generate a weekly averaged global SST analysis. We use linear interpolation to generate daily fields from this weekly data. MK02 used an earlier version of this Reynolds dataset (Reynolds and Smith 1994) to examine MJO-related SST variability in the east Pacific.

We compare TMI SST at the 1° × 1° grid cell centered at 8°N, 95°W to 1-m ocean temperature from the 8°N, 95°W TAO (McPhaden et al. 1998) moored buoy in the east Pacific during 2000–04. Buoy data are processed by constructing daily means from 20-min resolution data and then smoothing using a 3-day running average for consistency with the TMI data. Although we only show such a comparison for the 8°N, 95°W buoy (Fig. 2), the nature of the TAO–TMI temperature comparison is similar at other buoy sites in the east Pacific. The TMI and TAO temperature time series are shown in Fig. 2a, and 30–90-day bandpass-filtered TAO and TMI intraseasonal temperature anomalies are
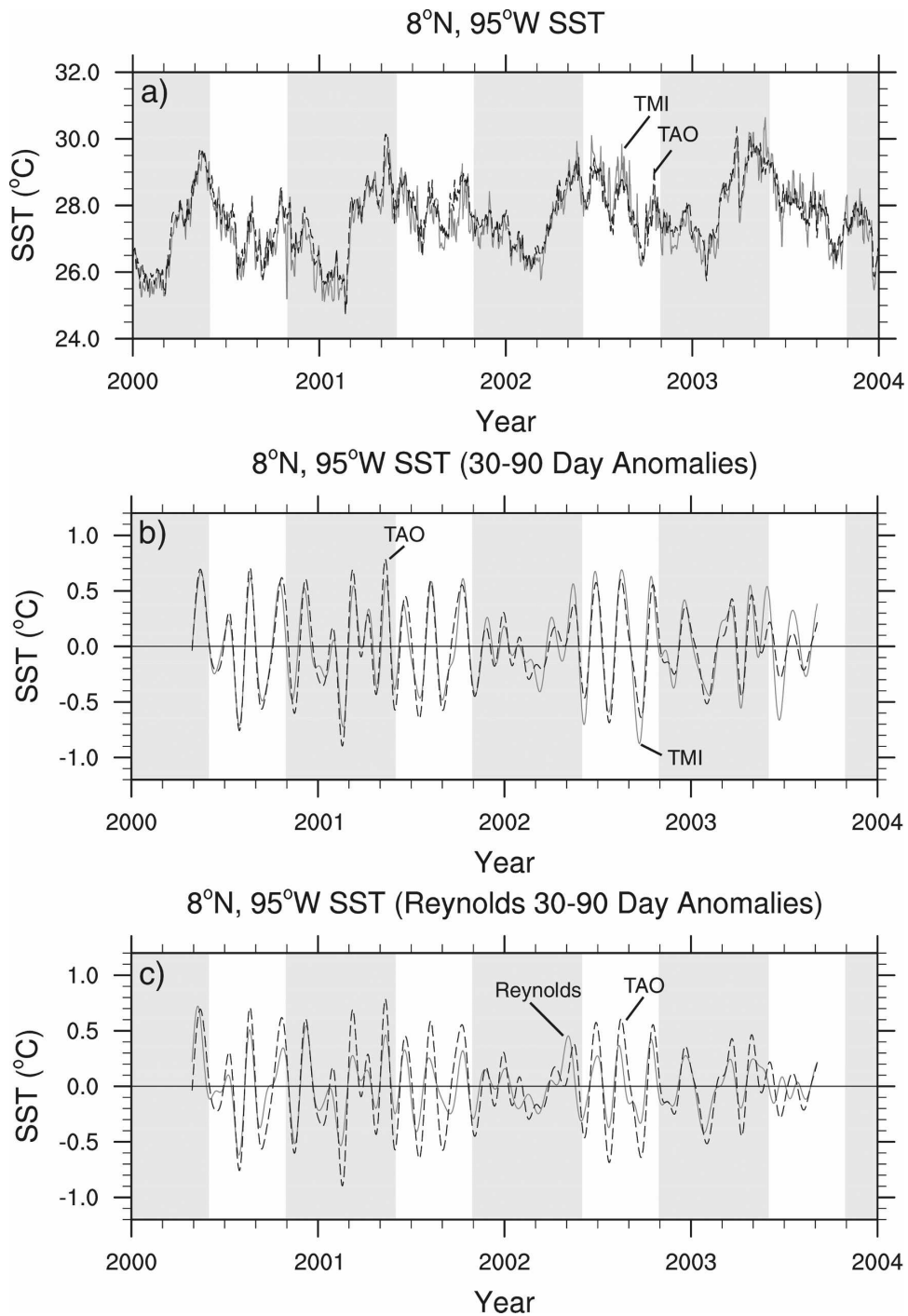
FIG. 2. (a) Unfiltered 8°N, 95°W TAO buoy 1-m depth temperature (black dashed) and TMI SST (gray solid), (b) 30–90-day bandpass-filtered 8°N, 95°W TAO buoy 1-m depth temperature (black dashed) and TMI SST (gray solid), and (c) 30–90-day bandpass-filtered 8°N, 95°W TAO buoy 1-m depth temperature (black dashed) and Reynolds SST (gray solid) June–October periods are highlighted in white, and gray shading covers the rest of the year.

shown in Fig. 2b. Reynolds and TAO intraseasonal temperature anomalies are compared in Fig. 2c. Intraseasonal TMI SST and buoy temperature anomalies generally agree well in amplitude and phase. Both SST time series have an intraseasonal variance of $0.12°C^2$. Intraseasonal Reynolds SST variance at the buoy site is only $0.05°C^2$, indicating that the Reynolds SST product used in MK02 underestimates the amplitude of intraseasonal SST variability in the east Pacific warm pool. Comparison between TMI and AMSR-E intraseasonal SST variance over a broader region of the east Pacific warm pool during 2003–05 also indicates good agreement (not shown), lending further confidence in the amplitude of intraseasonal SST variability produced by TMI.

Figure 2b indicates that TMI and buoy SST anomalies do not always agree in amplitude for specific events. Because TMI measures skin temperature and the buoy measures 1-m ocean temperature (which is more indicative of bulk temperature of the mixed layer), incomplete diurnal sampling by TMI may contribute to some of these differences. For example, daytime warm layers near the ocean surface in high-insolation and low-wind conditions can cause surface daytime ocean temperatures to vary substantially from those of the bulk mixed layer temperature (e.g., Schluessel et al. 1990; Ravier-Hay and Godfrey 1993; Fairall et al. 1996). Using only TMI nighttime or daytime passes in our analysis reduced the differences between TMI and TAO intraseasonal anomalies in some circumstances, but it did not generally improve the correspondence between TMI and TAO temperature anomalies. In some instances, the differences were exacerbated by subsampling using only TMI daytime or nighttime passes. Understanding the differences between the TMI and buoy temperature anomalies will remain a topic for future study. However, the superior spatial resolution and coverage of the TMI data provides a more realistic assessment of east Pacific intraseasonal SST evolution than in the TAO moorings or Reynolds SST (e.g., Chelton 2005; Chelton and Wentz 2005). The inadequacies of the Reynolds SST are clearly apparent from Fig. 2c.

b. Precipitation

We analyze intraseasonal precipitation variability to provide the context in which intraseasonal SST anomalies occur. As in the ME07 analysis of boreal summer intraseasonal precipitation variability in the east Pacific, we use precipitation fields from the TRMM 3B42, version 6, product that incorporates several satellite measurements, including the TMI and TRMM precipitation radar to calibrate infrared precipitation estimates

from geostationary satellites (e.g., Huffman et al. 2001). The precipitation data were downloaded from the Goddard Space Flight Center Distributed Access Archive System (accessed from http://trmm.gsfc.nasa.gov/). For consistency with the SST data, precipitation data were first averaged to a $1° \times 1°$ grid and then a 3-day running average was applied. Precipitation fields were used during June–October of 1998–2005, with an expanded May–October period for calculation of spectra.

3. Analysis of intraseasonal variance and coherence

a. Intraseasonal variance

Figure 3 shows intraseasonal SST and precipitation variance during June–October of 1998–2005, the months of which represent the period when influence of the MJO on the east Pacific warm pool is the strongest (Maloney and Hartmann 2001). Intraseasonal anomalies are defined using a linear nonrecursive bandpass filter with half-power points at 30 and 90 days.

Intraseasonal SST variance from TMI is shown in Fig. 3a and is characterized by three prominent maxima in the east Pacific. A longitudinally extended maximum occurs along 1°N, coincident with the latitudinal band demonstrated to contain strong tropical instability wave activity (e.g., Chelton et al. 2000). A second variance maximum occurs to the west of Costa Rica, centered near 9°N, 92°W. Here, the oceanic thermocline is shallow in association with the Costa Rica Dome, which is manifest at the surface as an SST minimum near 90°W relative to other longitudes along 10°N (Fig. 1). The climatology of the Costa Rica Dome is discussed in more detail by Xie et al. (2005). Intraseasonal variance in the 30–90-day band explains about 25% of the SST variance in the vicinity of the Costa Rica Dome. A third maximum in intraseasonal SST variance occurs near 19°N, 108°W at the northwestern edge of the east Pacific warm pool. Intraseasonal variance in the 30–90-day band explains about 30% of the SST variance in the vicinity of this northern variance maximum.

One question is whether the percent of SST variance explained by the 30–90-day band during the summer of 1998–2005 is representative of a longer record. To partially address this question, monthly mean fields from the Reynolds et al. (2002) SST product were used during an extended 1982–2005 period to determine whether 1998–2005 interannual variance in the Costa Rica Dome and northern edge of the warm pool is representative of the longer record. Interannual SST variance is of similar magnitude or slightly higher during 1998–2005 than in the extended record, lending confidence that the percent variance explained by the 30–90-day

30-90 Day TMI SST Variance

30-90 Day Reynolds SST Variance

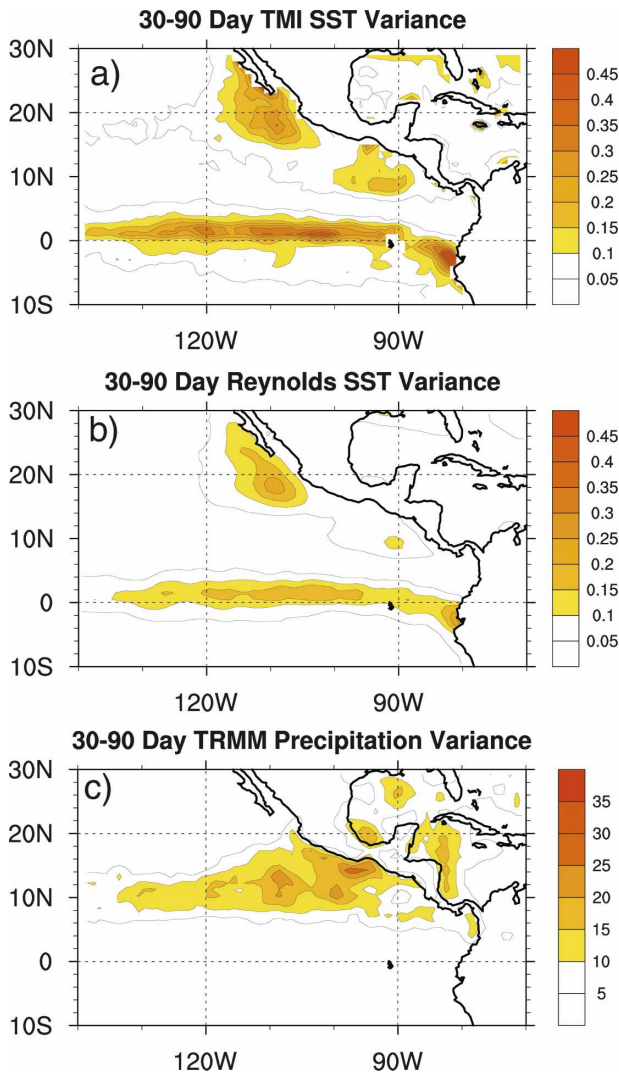### 30-90 Day TRMM Precipitation Variance

FIG. 3. The 30–90-day June–October (a) TMI SST, (b) Reynolds SST, and (c) TRMM precipitation variance calculated during 1998–2005. The contour interval is 0.05°C for SST and 5 mm^2 day^{-2} for precipitation.

band during 1998–2005 is representative of a longer period.

Figure 3b shows 30–90-day SST variance during 1998–2005 from the Reynolds et al. (2002) product. This SST product is similar to the Reynolds and Smith (1994) product used in MK02 to examine east Pacific intraseasonal SST variability. Intraseasonal SST variance is substantially reduced in Reynolds compared to TMI for the same 1998–2005 time period (Fig. 3a). An analysis of the ratio of Figs. 3a,b indicates that TMI SST variance is more than 50% higher than Reynolds over much of the warm pool—and more than twice as high near and to the west of the Costa Rica Dome. We will show that intraseasonal precipitation events are initi-

ated along 8°N from the Costa Rica Dome westward. The F statistic can be used to show that variance ratios of 2.0 and higher represent statistically significant variance differences at the 95% confidence level, where we have conservatively assumed that each 50 days of our June–October 1998–2005 record is an independent sample, giving 3 degrees of freedom per summer, for a total of 24 degrees of freedom over the 8-yr record. Our motivation for using 50 days to estimate degrees of freedom is that an MJO period is about 50 days, and Hendon and Salby (1994) found that adjacent MJO events are uncorrelated with each other.

To estimate the importance of the TMI SST variability to intraseasonal convection, we calculate the perturbation to the surface saturation moist static energy (MSE) that is generated by an SST anomaly of magnitude 1 standard deviation (using Fig. 3a) added to the mean June–October SST (Fig. 1) at each east Pacific location. Because of the nonlinear dependence of the Clausius–Clapeyron relation on temperature, the surface saturation specific humidity anomaly per unit SST perturbation is dependent on background SST.

Surface saturation MSE perturbations of greater than 1250 J kg^{-1} cover the entire east Pacific warm pool, with values near 2500 J kg^{-1} in the north part of the warm pool and near 2000 J kg^{-1} in the Costa Rica Dome (not shown here). Amplitudes are similar when examining east Pacific SST anomalies during composite MJO events (see Fig. 14). As a reference, Kemball-Cook and Weare (2001, their Fig. 9) and Kiladis et al. (2005, their Fig. 10) implied a build up of positive 1000-hPa MSE anomalies of 1000–1500 J kg^{-1} before the onset of MJO convection in the west Pacific and Indian Oceans. Clearly, surface latent and sensible heat fluxes must be considered in translating the effects of these SST anomalies to the boundary layer (e.g., ME07). However, the magnitude of the equilibrium boundary layer MSE anomaly associated with east Pacific TMI SST variations is sufficient to have important impacts on intraseasonal convection.

While the boundary layer is generally not in equilibrium with SST anomalies in the east Pacific, and processes in addition to air–sea exchange are important for regulating boundary layer moist static energy, we can use 2-m atmospheric fields from the 8°N, 95°W TAO mooring in the Costa Rica Dome to characterize the magnitude of boundary layer moist static energy anomalies on intraseasonal time scales relative to sea surface anomalies. Intraseasonal anomalies of 2-m moist static energy at 8°N, 95°W are of comparable magnitude to SST-derived buoy surface saturation moist static energy anomalies (~2000–2500 J kg^{-1}), and

generally lag SST anomalies by about one-quarter of a period (not shown here). This phase relationship is consistent with that expected from the theoretical ocean-coupling considerations of Sobel and Gildor (2003) and Maloney and Sobel (2004), whereby oceanic heat content builds before intraseasonal convective events, and ocean heat content anomalies are subsequently discharged to the atmosphere to support intraseasonal convection (Maloney and Sobel 2004, their Fig. 10). As implied by Fig. 3, the standard deviations of 30–90-day SST anomalies from TMI are higher than those from Reynolds in the east Pacific warm pool, implying considerable differences in the surface saturation MSE anomalies produced. The largest percentage differences are near and to the west of the Costa Rica Dome, where the standard deviation of intraseasonal TMI SST exceeds that from Reynolds by 90%, with comparable percentage increases in surface saturation MSE perturbations.

Intraseasonal precipitation variance provides a context for the analysis of SST anomalies. Boreal summer intraseasonal precipitation variability in the east Pacific warm pool was examined at length in ME07. Intraseasonal precipitation variance maximizes along 10°N (Fig. 3b), the axis of the Intertropical Convergence Zone, with a northward expansion of precipitation variance toward the Mexican and Central American coasts to the east of 110°W. Interestingly, a relative minimum in intraseasonal precipitation variance occurs where ocean temperatures are relatively cool in association with the Costa Rica Dome (Fig. 1), although SST variance is high there (Fig. 3a). Because the mixed layer of the Costa Rica Dome is shallow, relatively modest surface shortwave anomalies could be effective at forcing large changes in mixed layer temperature. It is also possible that factors other than surface shortwave anomalies associated with clouds may be important for generating SST variability in the Costa Rica Dome. ME07 showed that the Costa Rica Dome is characterized by strong wind anomalies during MJO events that produce large latent heat fluxes and momentum fluxes that can dynamically force the ocean. In addition to the east Pacific precipitation variance maxima, patches of relatively high intraseasonal precipitation variance occur in the far western Caribbean Sea, the Gulf of Mexico, and the Bight of Panama, regions where intraseasonal SST variability is relatively modest (Fig. 3a). These observations suggest that local SST variability is not essential for producing intraseasonal precipitation variability and that other factors such as wind evaporation and orographic forcing may be important for generating such precipitation variability.

b. Frequency spectra

Before calculation of the power spectra of boreal summer SST within the regions of high variance identified in Fig. 3a, the climatological seasonal cycle was removed from the data. The climatological seasonal cycle was generated by averaging data on each day of the year across all 8 yr of the record, and then applying six passes of a 1–2–1 filter to smooth the seasonal cycle, effectively a 9-day bandpass filter. Results are not sensitive to the precise means by which the seasonal cycle is removed. Removing the climatological seasonal cycle has the benefit of minimizing the influence of climatological intraseasonal oscillations such as the midsummer drought on the power spectra (e.g., Magaña et al. 1999), although the observed record clearly shows strong interannual variability in the strength and even existence of the midsummer drought that makes removal of the midsummer drought through removal of the climatological seasonal cycle somewhat incomplete (e.g., Curtis 2002; Small et al. 2007). However, as will be shown below, the dominant time scale of intraseasonal variability captured by the spectra is shorter than the 90–100-day time scale associated with the midsummer drought.

Spectra are calculated for each individual May–October period of the 8-yr record, and then averaged across all years. We use an expanded May–October period to calculate spectra. This expanded period and resulting narrower bandwidth of about $1/180$ days^{-1} allows better separation of MJO time scales from those of the midsummer drought. Sixteen degrees of freedom exist for each averaged spectral estimate. The average of the 1-day lag autocorrelation and square root of the 2-day lag autocorrelation are used to generate an estimate of the red noise background spectrum using the formula of Gilman et al. (1963), and 95% confidence limits on this background spectrum are calculated using the F statistic.

Power spectra of SST averaged over three $4° \times 4°$ boxes centered at 19°N, 108°W, 9°N, 92°W, and 1°N, 110°W are shown in Fig. 4. The northern two boxes coincide with the two east Pacific warm pool variance maxima described in Fig. 3a. Both warm pool power spectra exceed the confidence limits on the red noise spectrum at time scales of 50–60 days (Figs. 4a,b), consistent with time scales that characterize the MJO. The SST power spectrum at 1°N, 110°W indicates a significant peak at time scales of 20–35 days (Fig. 4c), periods characteristic of TIWs (Legeckis 1977; Qiao and Weisberg 1995; Chelton et al. 2000). Power at the 50–60-day time scales of interest in this study does not exceed the upper 95% confidence limit at the 1°N, 110°W box.
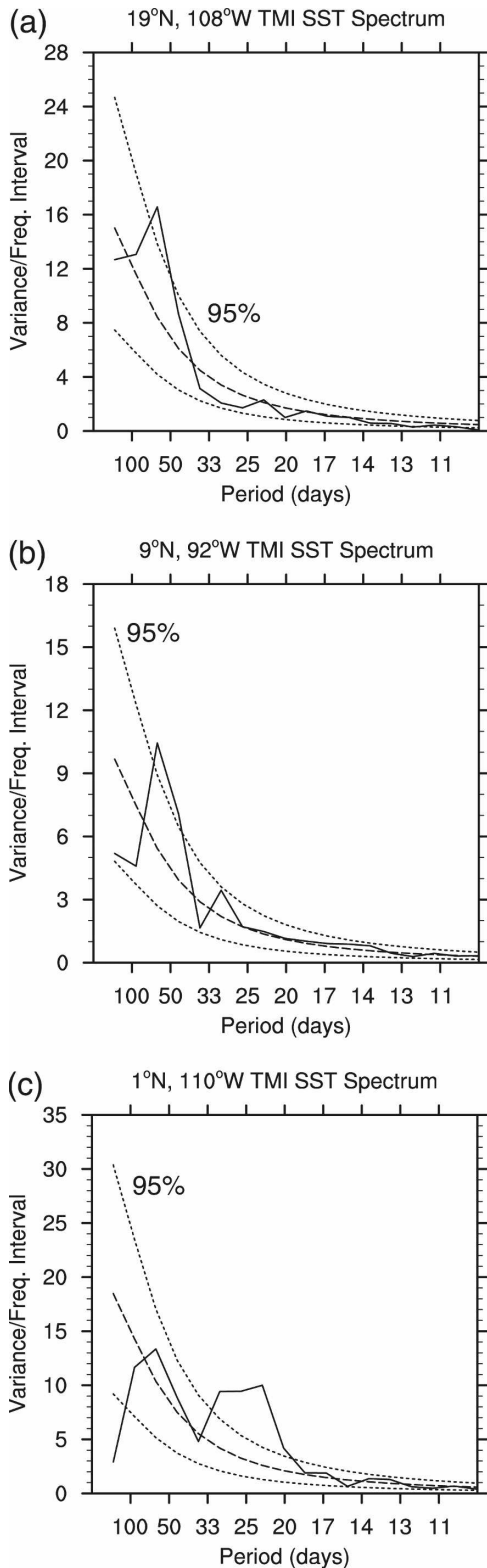
FIG. 4. Power spectrum of May–October TMI SST averaged over 4° × 4° boxes centered at (a) 19°N, 108°W, (b) 9°N, 92°W, and (c) 1°N, 110°W. The climatological seasonal cycle was removed before computation of the spectrum. Also shown are the red noise background spectrum and the 95% confidence limits on this background spectrum.
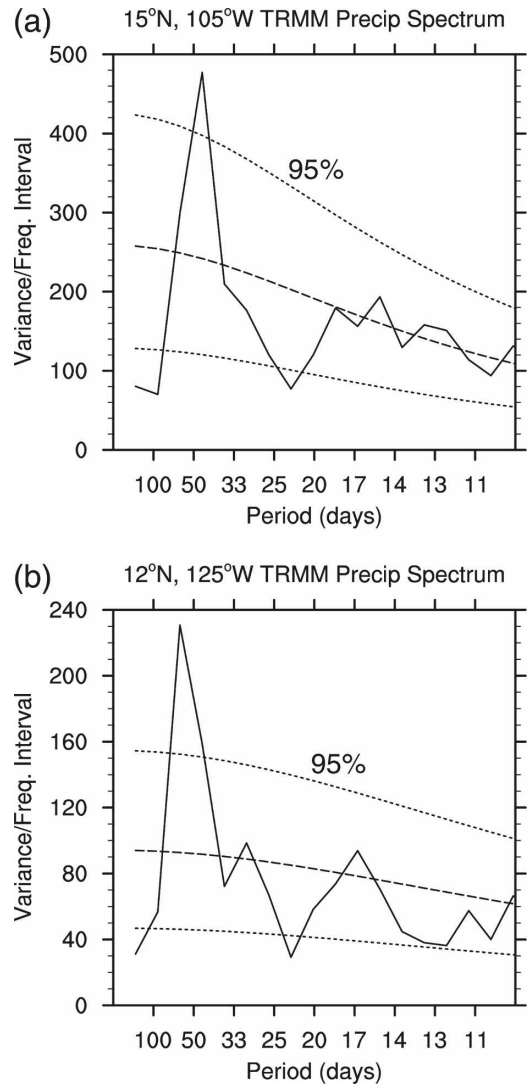

FIG. 5. Power spectrum of May–October TRMM precipitation averaged over 10° × 10° boxes centered at (a) 15°N, 105°W and (b) 12°N, 125°W. The climatological seasonal cycle was removed before computation of the spectrum. Also shown are the red noise background spectrum and the 95% confidence limits on this background spectrum.

May–October precipitation spectra are calculated for two 10° × 10° boxes centered at 15°N, 105°W and 12°N, 125°W (Fig. 5). Consistent with the warm pool SST spectra shown in Fig. 4, precipitation exhibits a significant spectral peak at 50–60-day time scales for both regions. The dominance of the 50–60-day time scale for precipitation is consistent with the behavior of MJO-related precipitation variability documented in ME07.

c. Analysis of coherence

While significant spectral power exists in the same intraseasonal frequency band across the east Pacific

warm pool in both SST and precipitation, the power spectra alone do not indicate whether such activity is coherent across the warm pool. An analysis of spectral coherence can diagnose the consistency of the phase relationship and amplitude ratio between the spectral components for two different time series when averaged across a frequency band. We conduct such an analysis of spectral coherence here, using as a reference time series the SST averaged over the $4° × 4°$ box centered at 9°N, 92°W. The climatological seasonal cycle was removed from all data before the analysis of coherence. We compute the coherence squared in the 30–90-day band between the reference time series and the remainder of the east Pacific during each individual May–October period, and then average over all 8 yr. A unit vector giving the phase relative to the reference time series is also derived for each May–October period. The phase vectors are then averaged over all 8 yr. The direction of the phase vector indicates the average phase relationship between the reference time series and the spatial location of the phase vector, and the magnitude of the average phase vector gives a measure of the consistency of the phase relationship across the 8 yr. A vector magnitude close to unity indicates that the phase relationship in the intraseasonal band is consistent across the 8 yr of data. A clockwise rotation of the vector indicates increasing phase, and thus the direction of phase propagation. For continuous phase propagation, anomalies with a higher phase peak later in time relative to those with lower phase.

Figure 6a shows the average May–October coherence squared in the 30–90-day band relative to SST at 9°N, 92°W and SST across the east Pacific. Similar results were found for the reference time series at 19°N, 108°W, and when precipitation is used as a reference time series rather than SST. The 95% significance level of squared coherence is 0.1. Regions of coherence squared greater than 0.3 are shown in color. Coherence squared exceeds 0.4 across most of the east Pacific warm pool, with intraseasonal SSTs along 10°N from the Costa Rica Dome westward being approximately in phase with those at the reference point. SSTs at the northern side of the warm pool lag those to the south by about ⅛ of a cycle (~1 week for a 50-day period). The phase relationship described by the vectors indicates that the intraseasonal SST anomalies are dominated by zonal spatial scales comparable to the east Pacific warm pool, consistent with the analysis of MK02, and much longer than would be obtained if the coherence were dominated by smaller-scale features such as oceanic eddies and Rossby waves, which have half wavelengths of 800 km and less and also contribute to boreal summer intraseasonal SST variability in the east Pacific (e.g.,
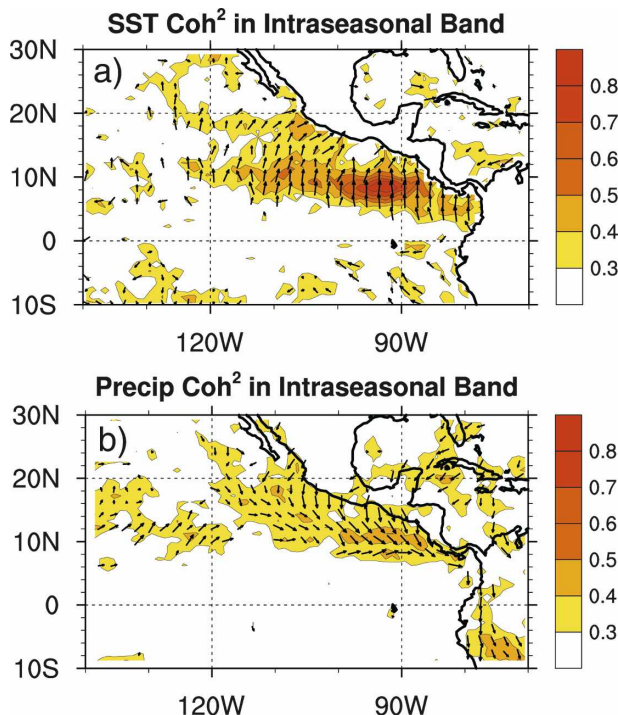

FIG. 6. Average May–October coherence squared in the intraseasonal band between a reference SST time series centered at 9°N, 92°W ($4° × 4°$ average) and maps of (a) SST and (b) precipitation. Coherence squared is computed individually for the eight summers and then averaged. Only regions of coherence squared greater than 0.3 are contoured. Also shown are phase vectors constructed as the average of the unit-length phase vectors from the eight individual summertime coherence estimates. Their amplitude gives an indication of the consistency of the phase relationship over all summers. Phase propagation is indicated by clockwise rotation.

Wijesekera et al. 2005; Palacios and Bogard 2005; Farrar and Weller 2006). Interestingly, relatively low coherence is found between warm pool SSTs and equatorial SSTs, in contrast to the findings of MK02 that boreal summer intraseasonal anomalies in SST over the warm pool are associated with opposite-signed anomalies along the equator. (See also the related discussion in section 5.)

Figure 6b shows the coherence squared and phase in the intraseasonal band between precipitation and the reference SST time series at 9°N, 92°W. Coherence squared between SST and precipitation is greater than 0.3 across the warm pool, with precipitation lagging 9°N, 92°W SST by a bit less than ¼ of a cycle near the reference point to ½ of a cycle near the northern edge of the warm pool. The rotation of the phase vectors indicates northward progression of precipitation anomalies. The phase of precipitation switches sign to the west of 120°W, consistent with the finding of ME07

that MJO-related precipitation anomalies over the warm pool are out of phase with those to the west of 120°W.

4. Complex EOF analysis

Hilbert transform complex empirical orthogonal function analysis (e.g., Barnett 1983; Horel 1984) provides a useful tool for examining the propagation characteristics and covariability of intraseasonal SST and precipitation anomalies in the east Pacific warm pool during summertime. CEOF analysis is like standard EOF analysis, but instead of the covariance matrix being constructed from the time series at each grid point in the spatial domain of interest, it is constructed from the complex analytic function at each grid point consisting of the time series plus its quadrature function times i. An advantage to CEOF analysis is that a propagating signal can be represented by one CEOF, rather than a quadrature pair of empirical orthogonal functions (EOFs). We compute the temporal Hilbert transform (quadrature function) of 30–90-day bandpass-filtered SST and precipitation over the entire 1998–2005 record to construct the analytic signal. A covariance matrix for CEOF calculation is then generated using data during June–October of 1998–2005 by multiplication of the matrix containing the analytic function at all grid points with its complex conjugate. CEOFs were computed at all available grid cells within the spatial domain 10°S–30°N, 70°–140°W. The spatial CEOFs and amplitude time series that result from this calculation are complex, and spatial and temporal phase and amplitude information can be derived in a straightforward manner.

The spatial amplitude, local variance explained, and spatial phase for the leading CEOF for 30–90-day June–October SST are shown in Fig. 7. CEOF1 of SST explains 15% of the total variance over the domain shown in the figure and is separable using the criterion of North et al. (1982) from CEOF2 and CEOF3, which explain 10% and 8% of the variance, respectively. The spatial amplitude of CEOF1 exhibits two regions of high amplitude (Fig. 7a): one in the vicinity of the Costa Rica Dome (and extending westward) and a second at the northern edge of the warm pool. Both of these locations are characterized by local maxima in variance in Fig. 3a. CEOF1 explains more than 40% of the local 30–90-day SST variance at the northern variance maximum (Fig. 7b) and more than 60% of the local variance in the vicinity of the Costa Rica Dome and locations westward. The spatial phase in Fig. 7c is shown only where the local variance explained exceeds 10%. Both spatial and temporal phases for CEOF1 were adjusted
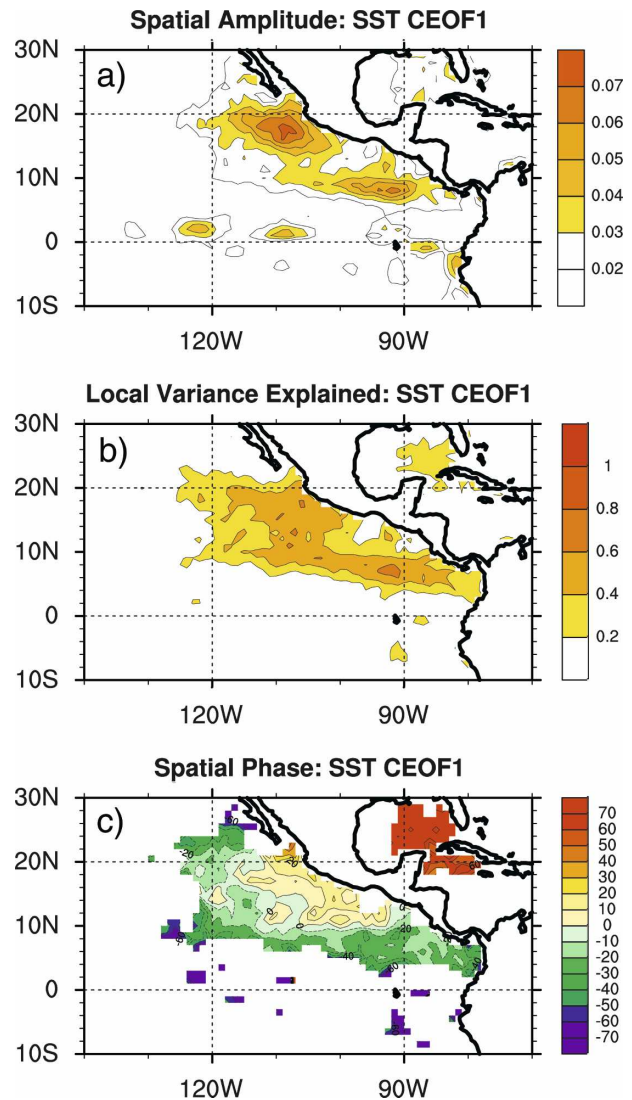

FIG. 7. (a) Spatial amplitude, (b) fraction of local variance explained, and (c) spatial phase corresponding to the first CEOF of June–October 30–90-day SST. The spatial amplitude was normalized in the calculation of the CEOFs. Increasing spatial phase indicated the direction of propagation for increasing temporal phase.

such that the amplitude maximum on the north side of the warm pool is collocated with a spatial phase of zero. The analysis of spatial phase indicates that Costa Rica Dome SST anomalies associated with CEOF1 lead those at the northern edge of the warm pool by about 40 degrees of phase, or about 6 days for a 50-day cycle, consistent with the phase lag shown in the analysis of coherence in Fig. 6a. SST anomalies in the Costa Rica Dome are approximately in phase with those westward along 8°N.

CEOF1 for 30–90-day precipitation shown in Fig. 8 explains 26% of the total variance within the domain
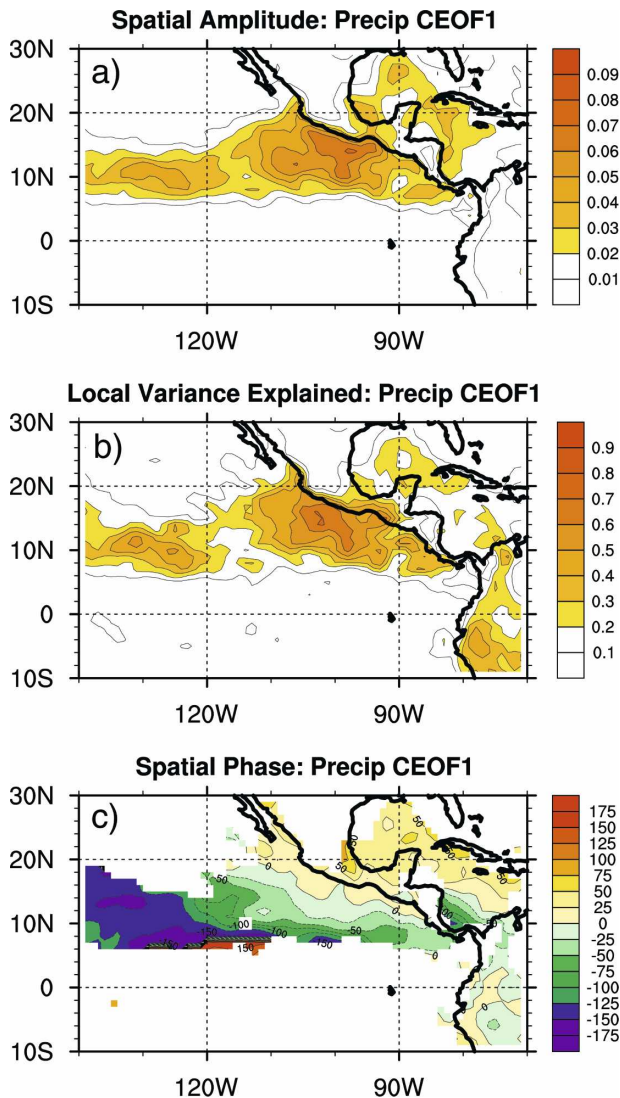
FIG. 8. Same as Fig. 7, but for precipitation.

shown, compared to 10% and 7% for CEOF2 and CEOF3, respectively. Amplitude associated with precipitation CEOF1 is highest over the east Pacific warm pool (Fig. 8a), with a secondary maximum in the ITCZ to the west of 120°W. The local variance explained by CEOF1 exceeds 60% over parts of the warm pool (Fig. 8b) and peaks at 50% to the west of 120°W. The spatial phase of precipitation CEOF1 is set to zero at the same SST amplitude maximum in the northern part of the warm pool as for CEOF1 of SST. Figure 8c shows that the spatial phase of precipitation varies little in the center of the warm pool to the south of Mexico, albeit with suggestions of slow northward propagation when combined with increasing temporal phase. Precipitation in these central warm pool regions lags precipitation along 8°N to the east of 120°W by 50–100 degrees of phase

(1–2 weeks). Precipitation to the west of 120°W leads that in the warm pool by 125–150 degrees of phase. These spatial phase relationships for precipitation are consistent with those shown in the MJO composites of ME07 and with the analysis of coherence presented in Fig. 6.

The CEOFs for precipitation and SST compactly represent the coherence and phase relations between intraseasonal SST and precipitation in Fig. 6. Evidence that the leading CEOFs represent a coherent physical mode of variability can be directly quantified. Normalized temporal amplitudes for CEOF1 of precipitation (black solid) and SST (black dashed) are shown in Fig. 9. We can derive a time series for a given CEOF by multiplying the temporal amplitude by the cosine of temporal phase. The correlation between such CEOF time series derived for SST and precipitation is shown as the solid line in Fig. 10. The time series are correlated at -0.9 when the precipitation time series leads the SST time series by about a week, providing strong evidence that the leading CEOFs of precipitation and SST represent a single coherent physical mode of variability. Because 0° phase for both CEOFs was assigned to the location of the SST amplitude maximum on the north side of the warm pool (Fig. 7a), the correlation in Fig. 10 indicates that positive (negative) SST anomalies lag suppressed (enhanced) precipitation in the north part of the warm pool by about a week.

The temporal and spatial phase information for the leading CEOFs of SST and precipitation can be combined to determine the phase lag between positive (negative) SST anomalies and suppressed (enhanced) precipitation across the east Pacific. The results of this analysis are shown in Fig. 11. Phase information is displayed only where the local explained variance for both SST CEOF1 and precipitation CEOF1 exceeds 10%. The phase lags shown represent an average over June–October of all years. Positive (negative) SST anomalies lag suppressed precipitation everywhere across the warm pool, with the regions of largest SST variance (Fig. 3a) being characterized by lags of about 50–75 degrees of phase (about 7–10 days for a 50-day cycle). This phase relationship between precipitation and SST makes it plausible that surface shortwave anomalies, which likely accompany anomalies in precipitation, contribute to SST anomalies that are manifest a week later. The results of MK02 also support this hypothesis.

5. Relationship of intraseasonal SST variability to the MJO

a. MJO time series

As described in MK02, an MJO time series can be derived using empirical orthogonal function analysis of
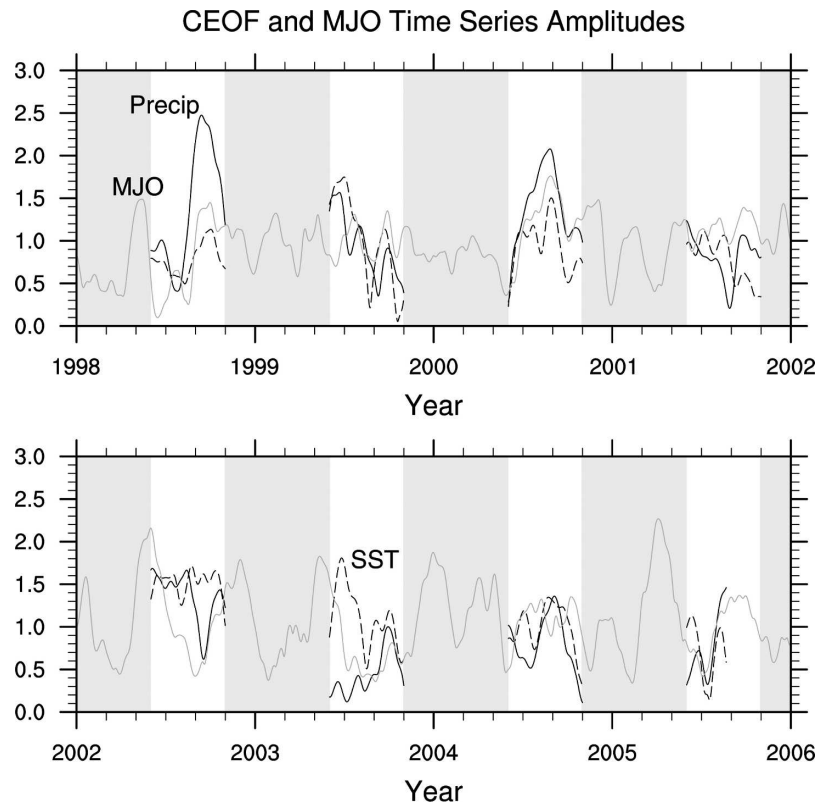
CEOF and MJO Time Series Amplitudes

FIG. 9. Amplitudes for precipitation CEOF1 (black solid), SST CEOF1 (black dashed), and the equatorial MJO time series (gray solid). CEOF amplitudes were normalized such that the mean over all 8 yr is one. June–October periods are highlighted in white, and gray shading covers the rest of the year. Note that CEOF amplitudes during September and October of 2005 are missing because of data loss associated with 30–90-day bandpass filtering that was applied before CEOF analysis.

equatorial zonal winds. EOF analysis is conducted on NCEP–NCAR reanalysis 1 (Kalnay et al. 1996) equatorial (5°N–5°S averaged) 30–90-day bandpass-filtered 850-hPa zonal winds during 1979–2005. Data across all seasons were used to conduct the EOF analysis. The two leading EOFs that explain a total of 59% of the intraseasonal equatorial zonal wind variance are shown in Fig. 12. The principal components (PCs) of these leading EOFs are correlated at 0.6 at a lag of 12 days, with PC2 lagging PC1. The leading EOFs can be interpreted as a quadrature pair that represents the eastward-propagating MJO (MK02; ME07). An MJO time series is defined by adding PC1 to the value of PC2 12 days later (Fig. 9, gray solid). As a check on the sensitivity of the MJO time series to the data-analysis product used, we also reconstructed the MJO time series using the 40-yr European Centre for Medium-Range Weather Forecasts (ECMWF) Re-Analysis (ERA-40) dataset (Uppala et al. 2005; not shown here). The ECMWF reanalysis-based MJO time series was virtu-

ally identical to that obtained using NCEP reanalysis 1. We also derived a comparable equatorial MJO time series using CEOF analysis of equatorial zonal winds at 850 hPa. The eastward-propagating variability associated with the MJO is captured by a single CEOF mode that is correlated at 0.98 with the EOF-based time series described above. Because the EOF-based time series has already been well documented in the literature and produces identical results to the CEOF index, we choose to use it for compositing.

Although derived using data across all seasons, we use the MJO time series during June–October to isolate boreal summer MJO variability. To determine how well this all-season time series represents the boreal summer MJO, we compare it to an objective measure of boreal summer intraseasonal variability derived using Eastern Hemisphere TRMM precipitation. The first two principal components of 30–90-day TRMM precipitation calculated over the domain 70°–180°E, 10°N–30°S during June–October (not shown here) represent
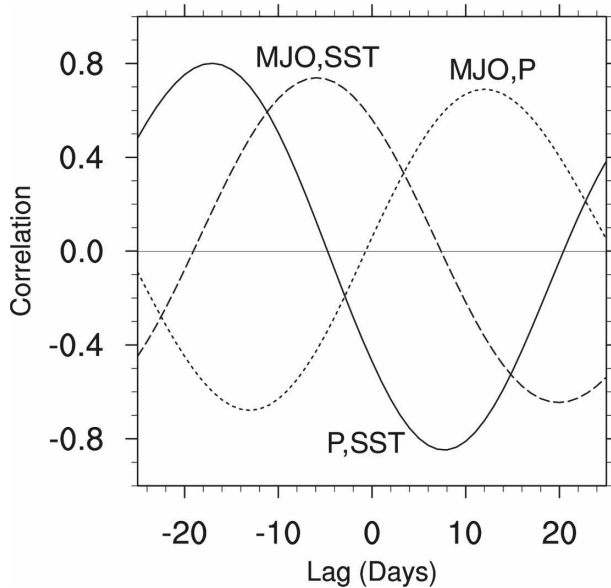
FIG. 10. Lag correlations for June–October among the time series of SST CEOF1, precipitation CEOF1, and equatorial MJO. Positive lags indicate that the time series listed on the left leads.

FIG. 12. EOF1 and EOF2 of the equatorial averaged (5°N–5°S) 850-hPa zonal wind as a function of longitude. Magnitudes were normalized in the computation of the EOFs.

a quadrature pair that captures the eastward and northward propagation of the MJO over the Eastern Hemisphere during boreal summer (e.g., Wang and Xie 1997; Lawrence and Webster 2002). The all-season equatorial MJO time series constructed from the EOFs in Fig. 12 is correlated at 0.8 with boreal summer Eastern Hemisphere PC1, indicating that the all-season MJO time series nicely represents boreal summer MJO variability. These results are consistent with the findings of Wheeler and Hendon (2004), who showed that a related all-season equatorial index derived from zonal wind and outgoing longwave radiation is able to capture MJO variability during boreal summer.
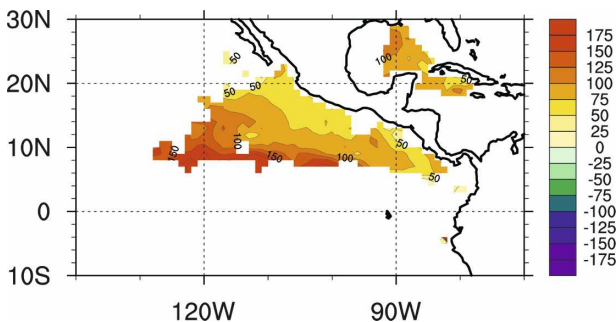

FIG. 11. The local phase angle by which positive (negative) SST anomalies lag suppressed (enhanced) precipitation, as determined from the temporal and spatial phases of SST CEOF1 and precipitation CEOF1.
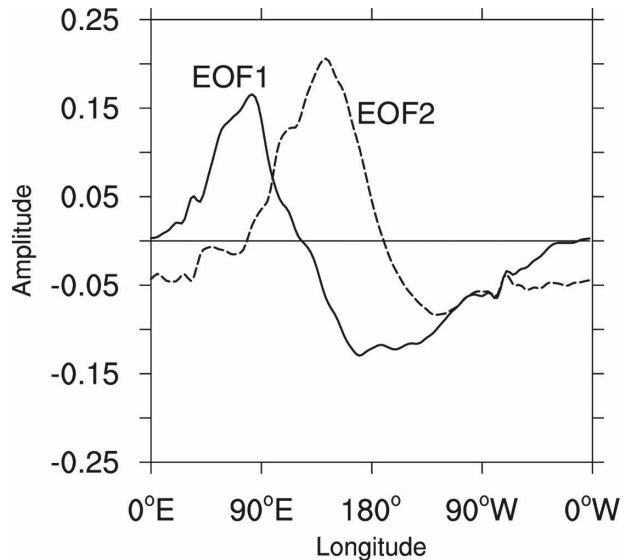
b. Relationship of the MJO time series to intraseasonal SST and precipitation

The MJO time series is multiplied by −1 for consistency with ME07 and then correlated during June–October of 1998–2005 with intraseasonal SST averaged over 4° × 4° boxes centered at 9°N, 92°W and 19°N, 108°W, and intraseasonal precipitation in a 10° × 10° box centered at 15°N, 105°W. These boxes are a subset of those used for the power spectra in Figs. 4, 5. Correlations with absolute values greater than 0.40 are significantly different from zero at the 95% confidence level. Significance was calculated by conservatively assuming that each 50-day period is an independent sample as described previously for the F test in section 3a.

The MJO time series achieves a correlation of +0.6 with SST at the two warm pool locations when SST leads the MJO time series by 10–15 days, and a correlation of −0.6 is produced when SST lags the MJO time series by 10–15 days (Fig. 13). As suggested in the analysis of coherence shown above (Fig. 6), SSTs in the vicinity of the Costa Rica Dome (9°N, 92°W) lead those at the northern edge of the warm pool (19°N, 108°W) by about 5 days. These results indicate that the MJO explains about 30%–40% of the boreal summer intraseasonal SST variance over the east Pacific warm pool and is likely a major contributor to the strong 50–60-day spectral peak observed over the warm pool during boreal summer (e.g., Fig. 4). Integrating the variance in excess of the background spectrum across
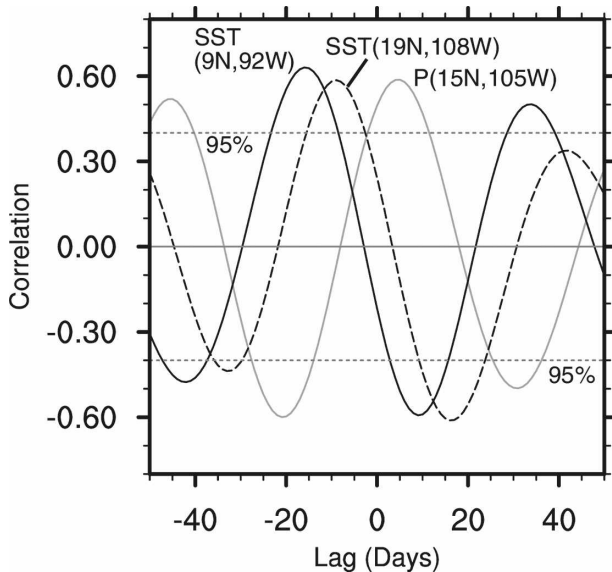
FIG. 13. Lag correlation of the equatorial MJO time series with June–October intraseasonal SST at 9°N, 92°W (black solid) and 19°N, 108°W (black dashed), and intraseasonal precipitation at 15°N, 105°W (gray solid). A positive lag indicates that the MJO time series leads.

the intraseasonal band, it can be shown that the variance associated with the spectral peaks of Fig. 4 exceeds that of the background spectra by about 40%–50%, thus contributing about 30% of the total variance.

The MJO time series is also significantly correlated with precipitation over the east Pacific warm pool with a magnitude of about 0.6. As a means of comparison, maximum correlations between the MJO time series and TRMM precipitation anomalies over the Eastern Hemisphere are about 0.7 (not shown here).

The correlations between the equatorial MJO time series and the time series derived from CEOF1 of precipitation and SST (as described above) are shown by the dashed lines in Fig. 10. The MJO time series is correlated with the SST CEOF1 time series at 0.7 when SST leads by 8 days, and it is correlated with the precipitation CEOF1 time series at 0.7 when the MJO time series leads by 12 days. The MJO time series thus explains about half of the variance of the CEOF time series, suggesting that these modes of variability are related to the MJO. However, because about half the variance of these CEOF-based time series cannot be explained by the MJO time series, it is possible that local processes unrelated to the MJO can generate intraseasonal variability resembling the leading CEOFs, or that local processes may help to modify MJO-related precipitation and SST variations over the east Pacific warm pool. This contention is supported by comparing the amplitude of the MJO time series to the CEOF1

amplitudes for precipitation and SST. A representative amplitude for the MJO time series can be derived from the principal components of the leading zonal wind EOFs (Fig. 12) as follows: $(PC1^2 + PC2^2)^{1/2}$. Figure 9 indicates that CEOF1 amplitudes for precipitation and SST do not always track the amplitude of the MJO time series. Such a possibility was also noted by Maloney and Hartmann (2001), who compared a local zonal wind index of east Pacific boreal summer intraseasonal variability to a global MJO time series. Further, Maloney and Esbensen (2003) used an energy budget analysis to show that local diabatic processes amplify MJO convection and wind anomalies over the east Pacific warm pool. Thus, the correlations shown in Fig. 10 suggest that the leading CEOFs of precipitation and SST are related to the MJO, although local east Pacific processes that produce feedbacks and variability render these correlations imperfect.

After multiplying the MJO time series by −1, a composite boreal summer MJO event can be generated by selecting June–October maxima in the MJO time series that exceed 1σ from zero. Sixteen such MJO events during June–October of 1998–2005 are selected using this method. A composite life cycle of the SST and precipitation variations associated with the MJO can then be derived by averaging precipitation and SST anomalies over all events at time lags of −20, −15, −10, −5, 0, +5, +10, and +15 days relative to the MJO time series maximum. Composite SST (color) and precipitation (contour) anomalies are shown in Fig. 14. Dotted regions indicate where the composite SST anomalies are determined to be statistically different from zero at the 95% confidence level using the t statistic with 16 degrees of freedom. Conclusions drawn from Fig. 14 and discussed below are similar when MJO time series minima are used to define MJO events. We also used the leading CEOFs of precipitation and SST to derive a composite life cycle (not shown), and the interpretation does not differ significantly from that described here.

As shown in ME07, suppressed precipitation maximizes over the bulk of the warm pool at days −20 and −15, although precipitation anomalies in the Costa Rica Dome become positive around day −15. Warm SST anomalies grow in the vicinity of the Costa Rica Dome from day −20 to −15 and on the northern edge of the warm pool from day −20 to −10. ME07 showed that the region near the Costa Rica Dome is accompanied by anomalous easterly winds, suppressed wind speed, and anomalous cyclonic shear during this period from day −20 to −15 when SST increases there. Positive SST anomalies reach their peak near the Costa Rica Dome about day −15 (+0.4°C) and over the northern section of the warm pool near day −10
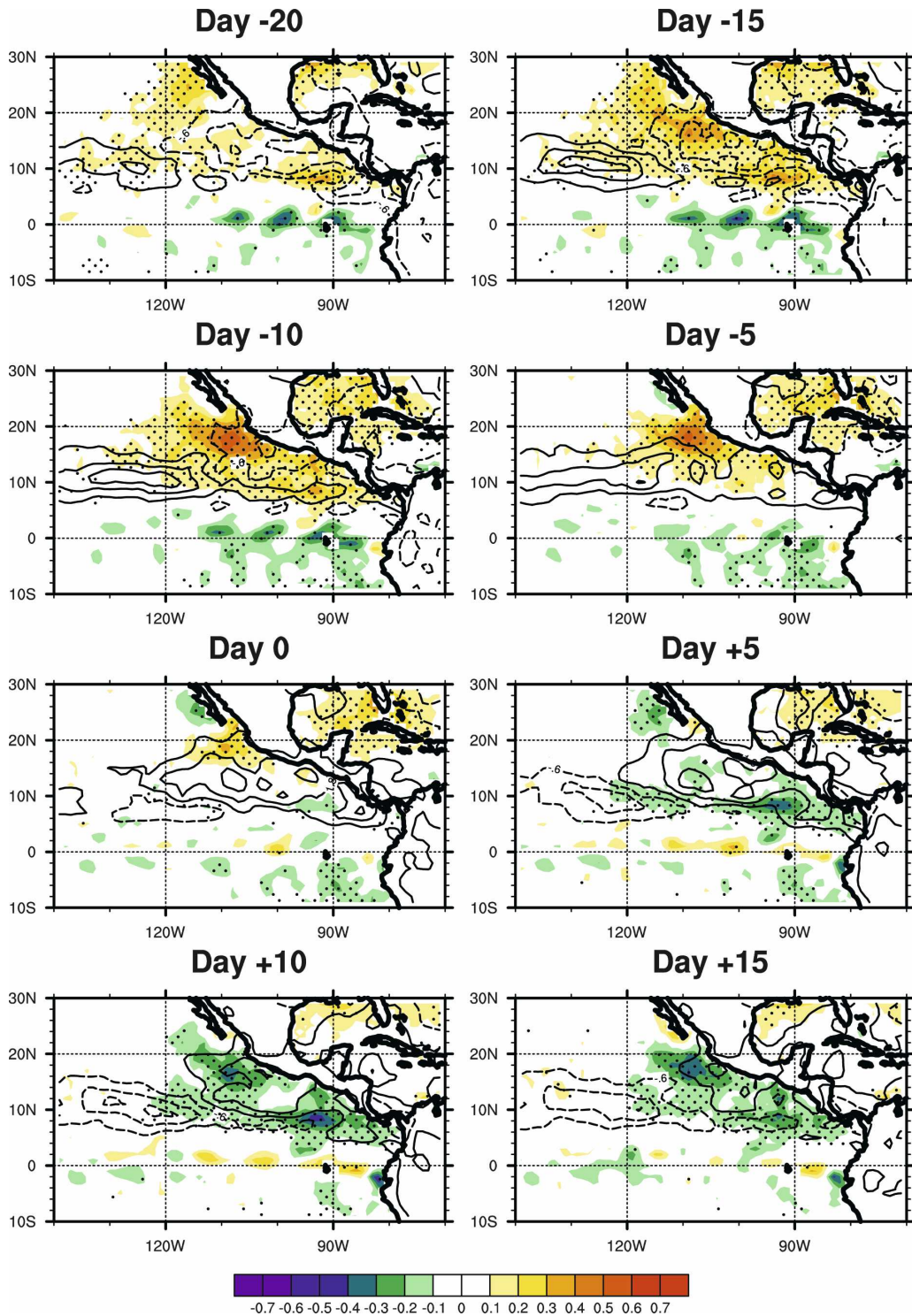
FIG. 14. Composite SST (fill) and precipitation (contours) anomalies as a function of lag in days relative to the MJO time series. The precipitation contour interval is 1.2 mm day^{-1}, starting at 0.6 mm day^{-1}, with negative contours dashed. Stippling indicates where SST anomalies are statistically different from zero at the 95% confidence level.

(+0.5°C). When SST is anomalously warm over the warm pool, small patches of significant cold SST anomalies occur near the equator, which are wavelike in character. Such an out-of-phase relationship was suggested from the smoothed Reynolds SST fields analyzed by MK02, although the equatorial SST anomalies found here from the high-resolution TMI data are relatively patchy and not spatially coherent. Further, no significant positive anomalies occur on the equator when warm pool SSTs are in their cold phase (e.g., see days +10 and +15). The analysis of coherence conducted above (Fig. 6) suggests weak coherence between warm pool and equatorial SST anomalies on intraseasonal time scales.

Positive precipitation anomalies at day −15 begin to grow in a narrow band along 8°N, with anomalies extending across a wider latitude band to the west of 110°W. These positive precipitation anomalies generally expand to cover the warm pool by day 0, and then shift northward. Warm pool precipitation anomalies reach their peak about day +5. Cold SST anomalies commence near the Costa Rica Dome around day 0, and then peak there about day +10 (−0.4°C). ME07 showed that the period of day 0 to +10 is associated with anomalous low-level westerly winds, enhanced wind speed, and anomalous anticyclonic shear in the vicinity of the Costa Rica Dome. Cold SST anomalies of about −0.4°C peak on the northern edge of the warm pool in the vicinity of 19°N, 108°W around day +15. Warm pool precipitation is in decline by day +15, with negative anomalies appearing along 8°N by days +10 to +15.

A time–longitude plot (not shown here) shows that near-equatorial composite SST anomalies in Fig. 14 propagate westward at 0.3 m s^{-1} with characteristic zonal wavelengths of about 1000 km, propagation speeds and spatial scales characteristic of TIWs (e.g., Chelton et al. 2000). Thus, it appears that TIWs contribute to the composite equatorial SST anomalies of Fig. 14. Strong TIWs that serendipitously coincide with MJO events, but are not necessarily related to the MJO, may cause composite equatorial SST anomalies to appear locally significant. Examination of individual events that comprise the MJO composite seems to confirm this hypothesis. A few of the 16 MJO events that comprise the composite are coincident with strong TIW activity and associated strong SST anomalies, which have a large influence on the composite SST field. Further, the correlation of the MJO time series with intraseasonal SST during boreal summer is not significant at the locations of prominent equatorial anomalies in Fig. 14. We also note that CEOF2 and CEOF3 of SST (not shown here) exhibit prominent equatorial ampli-

tude maxima and that CEOF3 appears to be associated with TIWs. These higher-order CEOFs are not significantly correlated with the MJO time series or with CEOF1 of precipitation or SST; thus, they appear to be independent of the MJO. However, the amplitudes of these higher-order CEOFs can be substantial during MJO events.

6. Discussion and conclusions

We now contrast the TMI-derived results found here with the results of MK02 that were derived using Reynolds SST. The results of this study differ significantly from MK02 in the following four ways: first, the higher-resolution TMI SST dataset used here during 1998–2005 allows a more accurate characterization of the amplitude of intraseasonal SST anomalies in the east Pacific than the Reynolds product used in MK02. Peak-to-peak TMI SST variations during a composite MJO life cycle are about 0.8°–1.0°C over the east Pacific warm pool, while Reynolds SST data produce composite peak-to-peak SST variations about half as large (Fig. 2; see also MK02). More generally, intraseasonal TMI SST variance is more than 50% higher than that of Reynolds over much of the east Pacific warm pool, and more than twice as high in the vicinity of the Costa Rica Dome (Fig. 3). The Costa Rica Dome is where intraseasonal precipitation is initiated and where TMI SST anomalies imply surface saturation moist static energy anomalies of greater than 2000 J kg^{-1}.

Second, the higher-resolution TMI product allows better localization of intraseasonal SST anomalies than in Reynolds. Our analysis indicates a strong local intraseasonal SST variance maximum in the Costa Rica Dome region, where northward-propagating intraseasonal precipitation anomalies are initiated. Another local SST variance maximum occurs on the north side of the east Pacific warm pool in the vicinity of 19°N, 108°W.

Third, the propagation characteristics of intraseasonal east Pacific SST and precipitation anomalies are examined using CEOF and coherence analysis, showing that intraseasonal SST and precipitation anomalies propagate northward in tandem in the east Pacific warm pool. Such northward-propagating covariability of precipitation and SST was not explored in MK02. SST and precipitation anomalies on the north side of the warm pool lag those in the Costa Rica Dome by 7–10 days.

Fourth, the spectral characteristics of east Pacific warm pool variability are explicitly examined in this study, showing significant 50-day spectral peaks in TMI SST and precipitation. Such an explicit examination of

spectral variance was not conducted in MK02, which was a more straightforward MJO composite study. A more minor difference between this study and that of MK02 is that equatorial SST variations that were notable during a composite MJO life cycle in MK02 using Reynolds are less prominent here, although patches of significant equatorial TMI SST anomalies are present in an MJO life cycle (e.g., Fig. 14, day −15). Strong TIWs that serendipitously coincide with MJO events, but are not likely related to the MJO, appear to contribute to these composite equatorial SST anomalies.

The findings of this study also show consistency with those of MK02, in some important respects. As in MK02, TMI SST during an MJO life cycle is approximately in quadrature with precipitation, with suppressed (enhanced) precipitation being followed by positive (negative) SST anomalies 7–10 days later. MK02 document a significant modulation of east Pacific warm pool SST and precipitation by the MJO, although a better characterization of the amplitude and spatial structure of such variability was achieved in this study using high-resolution TMI SST and TRMM precipitation datasets. The MJO, as defined by an equatorial time series, explains 30%–40% of the variance of intraseasonal TMI SST anomalies over the east Pacific warm pool during boreal summer.

Maloney and Kiehl (2002a) suggest that intraseasonal latent heat flux and surface shortwave radiation variations are important regulators of intraseasonal SST in the east Pacific warm pool. The coupled atmosphere–ocean general circulation model experiments of Maloney and Kiehl (2002b) suggest that intraseasonal east Pacific warm pool SST variations of amplitude even less than observed in our study may be important for producing observed east Pacific precipitation variability. Future work will examine the coupled oceanic and atmosphere processes responsible for regulating intraseasonal SST in the east Pacific. The EPIC2001 enhanced monitoring period of 2000–03 and the corresponding enhanced observations at the 8°N, 95°W, 10°N, 95°W, and 12°N, 95°W TAO buoys will be useful for examining the oceanic and atmospheric processes associated with intraseasonal SST variability near the Costa Rica Dome. The subsurface measurements at these buoys will also help determine how ocean dynamics contribute to MJO-related SST variability in the east Pacific warm pool. Substantial wind stress and wind stress curl anomalies occur in the east Pacific warm pool during MJO events (e.g., ME07). Surface stress fields from the SeaWinds scatterometer on QuikSCAT will be useful for analyzing the atmospheric forcing of ocean dynamics during MJO events.

Similar to what we observe in the east Pacific, no-table northward propagation of intraseasonal precipitation and SST anomalies also occurs in the South Asian monsoon system during boreal summer. Indian Ocean SST warming and associated boundary layer moist static energy increases to the north of the main intraseasonal convective center have been hypothesized to be important to northward propagation (e.g., Vecchi and Harrison 2002; Fu and Wang 2004). Positive SST anomalies similarly occur to the north of enhanced intraseasonal precipitation in the east Pacific warm pool (e.g., Fig. 14). While we have not explicitly analyzed the northward propagation of surface latent heat flux and shortwave radiation anomalies, surface wind speed anomalies analyzed in ME07 and the precipitation anomalies observed in this study are of the right sense to produce SST warming to the north of enhanced precipitation through their impacts on surface latent heat flux and shortwave radiation. Recent analyses also suggest that positive vertical vorticity anomalies are generated to the north of enhanced east Pacific MJO convection through vortex tilting in the presence of mean vertical zonal wind shear (X. Jiang 2007, personal communication). Such vorticity generation has been proposed as a northward-propagation mechanism for intraseasonal precipitation in the Indian Ocean (e.g., Jiang et al. 2004). Future work is necessary to assess these northward-propagation mechanisms for the east Pacific warm pool.

The strong local intraseasonal SST variability we observe in the east Pacific warm pool, theoretical work that suggests air–sea coupling can produce local intraseasonal oscillations of a recharge–discharge character (e.g., Sobel and Gildor 2003), and prominent northward propagation in SST and precipitation raise interesting questions about remote (e.g., from the west Pacific) versus local control of east Pacific intraseasonal variability. Several possibilities exist for how east Pacific and Eastern Hemisphere intraseasonal variability interact: 1) east Pacific intraseasonal variability with a 50-day time scale is locally generated, and any statistical relationship with Eastern Hemisphere intraseasonal variability is purely fortuitous; 2) in isolation, the east Pacific and Eastern Hemisphere would produce independent 50-day modes of variability. However, because they share a common time scale, east Pacific variability synchronizes with that in the Eastern Hemisphere because of rapid eastward communication in the tropical Pacific atmosphere; and 3) east Pacific warm pool 50-day variability is entirely forced from the Eastern Hemisphere. Given the significant correlation we observe between an equatorial MJO index and east Pacific precipitation and SST anomalies (e.g., Figs. 10, 13), the first possibility above appears unlikely. The third

possibility could be tested in a suitable east Pacific regional modeling study, in which the east Pacific domain is alternately forced with and without the influence of intraseasonal dynamical fields propagating from the lateral boundaries. Recent experiments with the regional ocean–atmosphere model developed at the University of Hawaii's International Pacific Research Center (Xie et al. 2007) suggest that this model can simulate east Pacific intraseasonal precipitation and SST variability with realistic amplitude and propagation characteristics (J. Small 2007, personal communication). Sensitivity tests could be conducted with such a model to test the importance of local versus remote control of east Pacific intraseasonal variability.

REFERENCES

Barnett, T. P., 1983: Interaction of the monsoon and Pacific trade wind system at interannual time scales. Part I: The equatorial zone. *Mon. Wea. Rev.,* **111,** 756–773.

Bhat, G. S., G. A. Vecchi, and S. Gadgil, 2004: Sea surface temperature of the Bay of Bengal derived from the TRMM Microwave Imager. *J. Atmos. Oceanic Technol.,* **21,** 1283–1290.

Chelton, D. B., 2005: The impact of SST specification on ECMWF surface wind stress fields in the eastern tropical Pacific. *J. Climate,* **18,** 530–550.

——, and F. J. Wentz, 2005: Global microwave satellite observations of sea surface temperature for numerical weather prediction and climate research. *Bull. Amer. Meteor. Soc.,* **86,** 1097–1115.

——, ——, C. L. Gentemann, R. A. deSzoeke, and M. G. Schlax, 2000: Microwave SST observations of transequatorial tropical instability waves. *Geophys. Res. Lett.,* **27,** 1239–1242.

——, and Coauthors, 2001: Observations of coupling between surface wind stress and sea surface temperature in the eastern tropical Pacific. *J. Climate,* **14,** 1479–1498.

Curtis, S., 2002: Interannual variability of the bimodal distribution of summertime rainfall over Central America and tropical storm activity in the far-eastern Pacific. *Climate Res.,* **22,** 141–146.

de Szoeke, S. P., and C. S. Bretherton, 2005: Variability in the southerly flow into the eastern Pacific ITCZ. *J. Atmos. Sci.,* **62,** 4400–4411.

Enfield, D. B., 1987: The intraseasonal oscillation in east Pacific sea levels: How is it forced? *J. Phys. Oceanogr.,* **17,** 1860–1876.

Fairall, C. W., E. F. Bradley, J. S. Godfrey, G. A. Wick, J. B. Edson, and G. S. Young, 1996: Cool-skin and warm-layer effects on sea surface temperature. *J. Geophys. Res.,* **101,** 1295–1308.

Farrar, J. T., and R. A. Weller, 2006: Intraseasonal variability near 10°N in the eastern tropical Pacific Ocean. *J. Geophys. Res.,* **111,** C05015, doi:10.1029/2005JC002989.

Fu, X., and B. Wang, 2004: Differences of boreal summer intraseasonal oscillations simulated in an atmosphere–ocean coupled model and an atmosphere-only model. *J. Climate,* **17,** 1263–1271.

Gentemann, C. L., F. J. Wentz, C. A. Mears, and D. K. Smith, 2004: In situ validation of Tropical Rainfall Measuring Mission microwave sea surface temperatures. *J. Geophys. Res.,* **109,** C04021, doi:10.1029/2003JC002092.

Gilman, D., P. Fuglister, and J. M. Mitchell, 1963: On the power spectrum of red noise. *J. Atmos. Sci.,* **20,** 182–184.

Harrison, D. E., and G. A. Vecchi, 2001: January 1999 Indian Ocean cooling event. *Geophys. Res. Lett.,* **28,** 3717–3720.

Hashizume, H., S.-P. Xie, W. T. Liu, and K. Takeuchi, 2001: Local and remote atmospheric response to tropical instability waves: A global view from space. *J. Geophys. Res.,* **106,** 10 173–10 185.

Hendon, H. H., 2000: Impact of air–sea coupling on the Madden–Julian oscillation in a general circulation model. *J. Atmos. Sci.,* **57,** 3939–3952.

——, and M. L. Salby, 1994: The life cycle of the Madden-Julian oscillation. *J. Atmos. Sci.,* **51,** 2225–2237.

Higgins, R. W., and W. Shi, 2001: Intercomparison of the principal modes of interannual and intraseasonal variability of the North American monsoon system. *J. Climate,* **14,** 403–417.

Horel, J. D., 1984: Complex principal component analysis: Theory and examples. *J. Appl. Meteor.,* **23,** 1660–1673.

Huffman, G. H., R. F. Adler, M. M. Morrissey, D. T. Bolvin, S. Curtis, R. Joyce, B. McGavock, and J. Susskind, 2001: Global precipitation at one-degree daily resolution from multisatellite observations. *J. Hydrometeor.,* **2,** 36–50.

Jiang, X., T. Li, and B. Wang, 2004: Structures and mechanisms of the northward propagating boreal summer intraseasonal oscillation. *J. Climate,* **17,** 1022–1039.

Kalnay, E., and Coauthors, 1996: The NCEP/NCAR 40-Year Reanalysis Project. *Bull. Amer. Meteor. Soc.,* **77,** 437–471.

Kayano, M. T., and V. E. Kousky, 1999: Intraseasonal (30–60 day) variability in the global Tropics: Principal modes and their evolution. *Tellus,* **51A,** 373–386.

Kemball-Cook, S. R., and B. C. Weare, 2001: The onset of convection in the Madden–Julian oscillation. *J. Climate,* **14,** 780–793.

Kiladis, G. N., K. H. Straub, and P. T. Haertel, 2005: Zonal and

vertical structure of the Madden–Julian oscillation. *J. Atmos. Sci.,* **62,** 2790–2809.

Lawrence, D. M., and P. J. Webster, 2002: The boreal summer intraseasonal oscillation: Relationship between northward and eastward movement of convection. *J. Atmos. Sci.,* **59,** 1593–1606.

Legeckis, R., 1977: Long waves in the eastern equatorial Pacific Ocean: A view from a geostationary satellite. *Science,* **197,** 1179–1181.

Lorenz, D. J., and D. L. Hartmann, 2006: The effect of the MJO on the North American monsoon. *J. Climate,* **19,** 333–343.

Madden, R., and P. R. Julian, 2005: Historical perspective. *Intraseasonal Variability in the Atmosphere-Ocean Climate System,* K. M. Lau and D. E. Waliser, Eds., Springer-Verlag.

Magaña, V., and E. Caetano, 2005: Temporal evolution of summer convective activity over the Americas warm pools. *Geophys. Res. Lett.,* **32,** L02803, doi:10.1029/2004GL021033.

——, J. A. Amador, and S. Medina, 1999: The midsummer drought over Mexico and Central America. *J. Climate,* **12,** 1577–1588.

Maloney, E. D., and S. K. Esbensen, 2003: The amplification of east Pacific Madden–Julian oscillation convection and wind anomalies during June–November. *J. Climate,* **16,** 3482–3497.

——, and ——, 2007: Satellite and buoy observations of boreal summer intraseasonal variability in the tropical northeast Pacific. *Mon. Wea. Rev.,* **135,** 3–19.

——, and D. L. Hartmann, 2000: Modulation of eastern north Pacific hurricanes by the Madden–Julian oscillation. *J. Climate,* **13,** 1451–1460.

——, and ——, 2001: The Madden–Julian oscillation, barotropic dynamics, and North Pacific tropical cyclone formation. Part I: Observations. *J. Atmos. Sci.,* **58,** 2545–2558.

——, and J. T. Kiehl, 2002a: MJO-related SST variations over the tropical eastern Pacific during Northern Hemisphere summer. *J. Climate,* **15,** 675–689.

——, and ——, 2002b: Intraseasonal eastern Pacific precipitation and SST variations in a GCM coupled to a slab ocean model. *J. Climate,* **15,** 2989–3007.

——, and A. H. Sobel, 2004: Surface fluxes and ocean coupling in the tropical intraseasonal oscillation. *J. Climate,* **17,** 4368–4386.

McPhaden, M. J., 2002: Mixed layer temperature balance on intraseasonal timescales in the equatorial Pacific Ocean. *J. Climate,* **15,** 2632–2647.

——, and Coauthors, 1998: The Tropical Ocean-Global Atmosphere observing system: A decade of progress. *J. Geophys. Res.,* **103,** 14 169–14 240.

Molinari, J., D. Knight, M. Dickinson, D. Vollaro, and S. Skubis, 1997: Potential vorticity, easterly waves, and eastern Pacific tropical cyclogenesis. *Mon. Wea. Rev.,* **125,** 2699–2708.

North, G. R., T. L. Bell, R. F. Cahalan, and F. J. Moeng, 1982: Sampling errors in the estimation of empirical orthogonal functions. *Mon. Wea. Rev.,* **110,** 699–706.

Qiao, L., and R. H. Weisberg, 1995: Tropical instability wave kinematics: Observations from the Tropical Instability Wave Experiment. *J. Geophys. Res.,* **100,** 8677–8693.

Palacios, D. M., and S. J. Bogard, 2005: A census of Tehuantepec and Papagayo eddies in the northeastern tropical Pacific. *Geophys. Res. Lett.,* **32,** L23606, doi:10.1029/2005GL024324.

Ravier-Hay, P., and J. S. Godfrey, 1993: A model of diurnal changes in sea surface temperature for the western equatorial Pacific. TOGA Notes 11, 5–8.

Raymond, D. J., C. S. Bretherton, and J. Molinari, 2006: Dynam-ics of the intertropical convergence zone of the east Pacific. *J. Atmos. Sci.,* **63,** 582–597.

Reynolds, R. W., and T. M. Smith, 1994: Improved global sea surface temperature analyses using optimum interpolation. *J. Climate,* **7,** 929–948.

——, N. A. Rayner, T. M. Smith, D. C. Stokes, and W. Wang, 2002: An improved in situ and satellite SST analysis for climate. *J. Climate,* **15,** 1609–1625.

——, C. Liu, T. M. Smith, D. B. Chelton, M. G. Schlax, and K. S. Casey, 2007: Daily high-resolution-blended analyses for sea surface temperature. *J. Climate,* **20,** 5473–5496.

Schluessel, P., W. J. Emery, H. Grassl, and T. Mammen, 1990: On the bulk-skin temperature difference and its impact on satellite remote sensing of sea surface temperature. *J. Geophys. Res.,* **95,** 13 341–13 356.

Sengupta, D., B. N. Goswami, and R. Senan, 2001: Coherent intraseasonal oscillations of ocean and atmosphere during the Asian summer monsoon. *Geophys. Res. Lett.,* **28,** 4127–4130.

Small, R. J. O., S. P. de Szoeke, and S.-P. Xie, 2007: The Central American midsummer drought: Regional aspects and large-scale forcing. *J. Climate,* **20,** 4853–4873.

Sobel, A. H., and H. Gildor, 2003: A simple time-dependent model of SST hot spots. *J. Climate,* **16,** 3978–3992.

Spillane, M. C., D. B. Enfield, and J. S. Allen, 1987: Intraseasonal oscillations in sea level along the west coast of the Americas. *J. Phys. Oceanogr.,* **17,** 313–325.

Uppala, S. M., and Coauthors, 2005: The ERA-40 re-analysis. *Quart. J. Roy. Meteor. Soc.,* **131,** 2961–3012.

Vecchi, G. A., and D. E. Harrison, 2002: Monsoon breaks and subseasonal sea surface temperature variability in the Bay of Bengal. *J. Climate,* **15,** 1485–1493.

Waliser, D. E., K. M. Lau, and J.-H. Kim, 1999: The influence of coupled sea surface temperatures on the Madden–Julian oscillation: A model perturbation experiment. *J. Atmos. Sci.,* **56,** 333–358.

Wang, B., and X. Xie, 1997: A model for the boreal summer intraseasonal oscillation. *J. Atmos. Sci.,* **54,** 72–86.

Wang, C., and D. B. Enfield, 2001: The tropical Western Hemisphere warm pool. *Geophys. Res. Lett.,* **28,** 1635–1638.

Wentz, F. J., C. Gentemann, D. Smith, and D. B. Chelton, 2000: Satellite measurements of sea surface temperature through clouds. *Science,* **288,** 847–850.

Wheeler, M. C., and H. H. Hendon, 2004: An all-season real-time multivariate MJO index: Development of an index for monitoring and prediction. *Mon. Wea. Rev.,* **132,** 1917–1932.

Wijesekera, H. W., D. L. Rudnick, C. A. Paulson, S. D. Pierce, W. S. Pegau, J. Mickett, and M. C. Gregg, 2005: Upper ocean heat and freshwater budgets in the eastern Pacific warm pool. *J. Geophys. Res.,* **110,** C08004, doi:10.1029/2004JC002511.

Xie, S. P., H. Xu, W. S. Kessler, and M. Nonaka, 2005: Air–sea interaction over the eastern Pacific warm pool: Gap winds, thermocline dome, and atmospheric convection. *J. Climate,* **18,** 5–20.

——, and Coauthors, 2007: A regional ocean–atmosphere model for eastern Pacific climate: Toward reducing tropical biases. *J. Climate,* **20,** 1504–1522.

Zhang, C., 2001: Intraseasonal perturbations in sea surface temperatures of the equatorial eastern Pacific and their association with the Madden–Julian oscillation. *J. Climate,* **14,** 1309–1322.